Synthesis of Hard Carbon-TiN/TiC Composites by Reacting Cellulose with $TiCl_4$ Followed by Carbothermal Nitridation/Reduction

Hang Cheng, Nuria Garcia-Araez, Andrew L. Hector* and Samantha Soulé

School of Chemistry, University of Southampton, Southampton SO17 1BJ, United Kingdom

Abstract: Titanium tetrachloride is reacted with hydroxide groups on cellulose (cotton wool) before firing to convert the cellulose to hard carbon. Hard carbon-nanocrystalline titanium nitride composites with a good distribution of the titanium across the fibrous hard carbon structure were obtained by firing the treated cellulose under nitrogen. Hard carbon-nanocrystalline titanium carbide composites were obtained by firing under argon. The composites were tested as anode materials for sodium ion batteries and the HC-TiN composite delivers a better capacity retention than that of hard carbon over 50 cycles. The synthesis method demonstrated here provides an effective route to composites of metal nitrides and carbides with carbon that may be of interest for other energy technologies as well as for sodium batteries.

INTRODUCTION

Transition metal nitrides/carbides are promising electrode materials in energy applications due to a combination of high electronic conductivity[1,2] with electrocatalytic activity or charge storage capabilities, with the latter sometimes due to surface oxide layers. MoN and WC exhibit high Pt-like electrocatalytic activities.[3,4] VN and TiC have been successfully applied in supercapacitors.[5,6] A series of transition metal nitrides (Cu_3N[7], Co_3N[8] and Fe_3N[8]) and transition metal carbide (Mo_2C[9]) have been explored as anode materials for lithium ion batteries (LIBs) and recently a number of metal nitrides (MN_x, M = Cu, Mn, Ni, Sn etc.) synthesized by our group[10-13] and the VN reported by Cui *et al.*[14] have shown promising electrochemical properties for sodium ion batteries. In several of these systems there is evidence that conversion reactions (reduction to the metal and sodium nitride) occur mainly at particle surfaces and hence that reducing particle size will be important in maximizing their capacities. Zhang *et al.*[15] reported Mo_2C as a sodium storage material with good cycling and rate performance.

Carbon-based composites in electrochemical applications provide good electrical conductivity and high chemical resistance. Carbon is routinely used as a conductivity additive in battery and supercapacitor electrode fabrication.[16,17] Carbon supported platinum metals and oxides in fuel cells preserve nanoparticle surface area whilst providing good conduction pathways.[18] Recently extensive work on supporting a range of materials on carbon to exploit these properties has been reported. For example, mesoporous TiN/C microfibers are more efficient than Pt/C for both the oxygen reduction and the oxygen evolution reaction in Li-O_2 cells.[19] Yousef *et al.*[20] embedded Co-TiC nanoparticles on carbon nanofibers and then used the composite for fuel cells and dye-sensitized solar cells. Composites for battery applications include Co_3O_4 on graphene with a reversible capacity of 935 mAh g^{-1} vs Li,[21] and Mo_2C nanoparticles encapsulated into a porous N-doped carbon matrix that achieved a capacity retention of 95.4% after 2500 cycles vs Na.[22]

A number of strategies have been used to synthesize carbon-supported metal nitrides and carbides. For instance, Zhu et al.[23] synthesized MoN@nitrogen-doped carbon electrocatalysts by decomposing a metal-organic framework to MoO_2-C followed by calcination under ammonia. Zhang et al.[24] deposited titanium nitride on carbon fibres using a sol-gel method and then applied this coating in flexible supercapacitors. Cao et al.[25] applied a solvothermal method followed by firing at 550 °C under an H_2-Ar mix to obtain Mo_2C-C hybrid nanospheres, displaying a better cyclic performance in LIBs than bulk Mo_2C.

Sodium-ion battery (SIB) research started with that on LIBs in the 1980s,[26-28] but while LIBs have achieved massive commercial success, effort into SIBs was minimal for the following two decades. There are potential future problems with the growing cost of lithium as usage of LIBs in transport and large-scale storage is increasing.[29] The low cost and abundant supply of sodium[30,31] have driven a significant recent upturn SIB interest in the last few years, with 4 papers published in 2010 and 1464 in 2018 (Web of Science Core Collection[32] 25th March 2019 with topic of "sodium ion batter*"). The best-known anodic host material in LIBs, graphite,[33,34] does not intercalate sodium to any significant degree due to an ionic radius 55% larger than that of lithium. Hard carbon (HC) is an attractive alternative to graphite for SIBs, with a good conductivity and fairly high reversible capacity at low voltage.[35] HC is obtained by pyrolysis of various precursors including resorcinol-formaldehyde,[36] glucose[37] and peat moss.[38] Cotton wool is a promising low cost, renewable precursor for synthesis of hard carbon.[39] Our interest is in producing composite materials with hard carbon to improve its capacity and capacity retention with cycling.

Herein, we report an effective method to obtain HC-TiN or HC-TiC composites by reacting a reactive metal precursor with cellulose before firing to convert the cellulose to HC. Carbothermal nitridation under N_2 gas yielded HC-TiN whereas carbothermal reduction under argon produced HC-TiC. Both composites show similar first cycle capacities to HC, but the titanium nitride composite delivers a better capacity retention (85.2%) after 50 cycles than that of hard carbon (74.3 %). We expect the synthesis method demonstrated here to provide an effective route to composites with other metal nitrides and carbides for sodium cell and other energy technologies.

EXPERIMENTAL

The composites were synthesized by reacting cotton wool with $TiCl_4$ then firing in nitrogen or argon. Cotton wool (5 g, Fisher Scientific) was dried *in vacuo* overnight. It was then placed into a flask under N_2 and covered with hexane (200 mL, Fisher Scientific, distilled from sodium/benzophenone ketyl ether) followed by addition of different volumes of $TiCl_4$ (between 0 and 0.5ml, Sigma-Aldrich, 99.9% trace metals basis). The mixture was heated to reflux overnight and then the solvent and any remaining precursor was removed *in vacuo*. The dried material was transferred into a furnace tube in the glove box and then fired under nitrogen or argon. Firing was carried out with a temperature ramp of 4 °C min^{-1} to 1400 °C and this temperature was maintained for 2 h. Pure hard carbon (HC) samples were synthesized for comparison using the same steps but without adding the $TiCl_4$ during synthesis.

Powder X-ray diffraction (XRD) patterns were collected in 0.7 mm silica capillaries with parallel Cu-K_α X-rays using a Rigaku Smartlab. XRD data analysis used the Rigaku PDXL2 and GSAS packages.[40] Raman spectra were collected with a Renishaw inVia Ramascope operating at 785 nm with an energy of 7.08 mW. Raman peak analysis used WiRE software, a linear baseline correction and curve-fitting of the three peaks

(G, D and D3) using Gaussian and Lorentzian functions. Thermogravimetric analysis (TGA) was measured with a TG 209 F1 Libra with a ramp rate of 10 °C min^{-1} with flowing gas mixture of Ar (50 ml min^{-1}) and O_2 (20 ml min^{-1}). Scanning electron microscopy (SEM) used a Philips XL30 and a Jeol JSM6500 with 10 kV accelerating voltage. Energy dispersive X-ray (EDX) analysis used a Thermofisher Ultradry detector. Transmission electron microscopy (TEM) used a FEI Tecnai T12 (80 kV). X-ray photoelectron spectroscopy (XPS) was carried on a Thermo Nexsa with Al K_α X-rays. XPS data analysis was conducted from the Casa XPS software package. The XPS binding energy scale was calibrated to graphitic carbon at 284.6 eV. Core peaks were fitted with nonlinear Shirley-type background.[41] Peak positions and areas were optimized by a weighted least-squares fitting method using 70% Gaussian and 30% Lorentzian line shapes. The surface areas were calculated by the Brunauer-Emmet-Teller (BET) method from nitrogen adsorption/desorption isotherms obtained on a Micromeritics Tristar II surface area analyzer.

Working electrodes were prepared from inks produced using 0.2 g of composite or HC with a polyvinylidene difluoride (Solvay) binder at a weight ratio of 95:5 %wt. These materials were mixed with N-methyl-2-pyrrolidone (0.5-0.6 mL, anhydrous, 99.5%, Sigma-Aldrich) to prepare a viscous ink, which was mixed with an homogenizer (running at speed of 10000, 15000 and 20000 revolutions per minute for 5, 3 and 2 min, respectively) and cast onto copper foil (0.0175 mm thick, Goodfellow Cambridge Ltd) using a K-bar of 200 μm. The ink was air dried before the foil was cut into 11 mm diameter discs, and then further dried under vacuum overnight. Typical mass loadings of electrodes prepared in this way were 2-2.5 mg cm^{-2}. 11 mm diameter discs of sodium (Sigma-Aldrich) were used as the counter and reference electrode. Two sheets of dried Whatman GF/D glass fiber (GE Healthcare Life Sciences) were used as the separator, soaked with 180 μL of the electrolyte which was made up from 1 M $NaClO_4$ (Alfa Aesar, anhydrous) in a mixture of ethylene carbonate (EC, Sigma-Aldrich, anhydrous, 99%) and diethyl carbonate (DEC, Sigma-Aldrich, anhydrous, ≥ 99%) in a 1:1 ratio in volume. All the electrochemical tests were conducted using Swagelok cells and all the cell assembly was carried out in an argon-filled glove box (Mbraun, H_20 < 0.1 ppm, O_2 < 0.1 ppm). Galvanostatic charge/discharge cycling was performed at 25 °C in the voltage range 5 mV to 2 V (vs. Na^+/Na) using a Biologic MPG potentiostat. Electrochemical impedance spectroscopies (EIS) were obtained in the frequency range from 0.05 Hz to 500 kHz at room temperature.

RESULTS AND DISCUSSION

Scheme 1 illustrates the synthesis process of the HC-TiN and HC-TiC composites. The main component in cotton wool is cellulose (~95%)[42], which is a polymer of β-D-glucose. The hydroxide groups on the cellulose are expected to react with the $TiCl_4$ to form C-O-Ti bonds with HCl as the byproduct. Initially reactions were carried out at room temperature since the $TiCl_4$ was expected to be highly reactive with these hydroxide groups, but it was found that titanium loadings on the cellulose were higher when the solution was refluxed. This may be related to poor wetting of the polar cellulose surfaces by the low polarity hexane solvent. Different volumes of $TiCl_4$ (Table 1) were added to obtain composites with various Ti loadings. After firing, composites of TiN or TiC with hard carbon were produced. The amount of the titanium-containing phase in these composites was measured by heating the samples in the TGA (supplementary information, Fig. S1) to remove the carbon and oxidize the titanium to TiO_2.

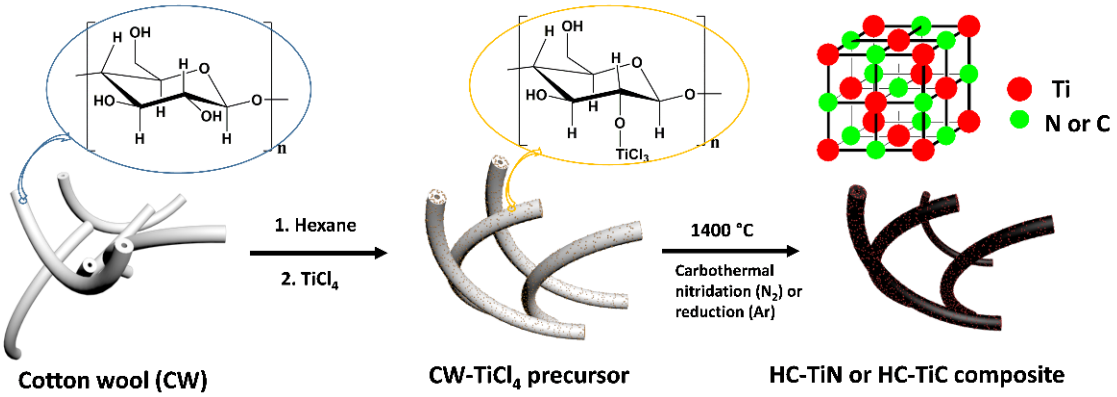

Scheme 1 The synthesis process used to make HC-TiN and HC-TiC composites.

Table 1 Physical parameters of HC-TiN and HC-TiC composites.

Sample	$TiCl_4$ used in synthesis (mL)	HC parameters d (002) (Å)	I_D/I_G	TiN/TiC parameters a=b=c (Å)	Crystallite size (Å)	Composite surface area (m^2/g)
HC-N_2[(1)]	0	3.842(7)	1.71	n/a	n/a	61
1.89% *wt* TiN	0.1 mL	3.887(5)	1.82	4.24714(4)	36(5)	111
8.57% *wt* TiN	0.2 mL	3.915(6)	1.86	4.24262(5)	179(8)	89
10.14% *wt* TiN	0.3 mL	3.939(5)	1.94	4.24599(3)	191(27)	79
15.15% *wt* TiN	0.4 mL	3.962(7)	1.97	4.24430(7)	239(5)	73
17.27% *wt* TiN	0.5 mL	3.964(5)	2.03	4.24113(7)	340(19)	71
HC-Ar[(2)]	0	3.803(5)	1.58	n/a	n/a	57
4.28% *wt* TiC	0.1 mL	3.934(5)	1.86	4.32272(2)	191(9)	92
8.65% *wt* TiC	0.2 mL	3.967(8)	1.97	4.304718(14)	314(5)	82
16.27% *wt* TiC	0.4 mL	3.988(5)	2.16	4.31932(3)	380(12)	41

[(1)] Hard carbon obtained under nitrogen gas; [(2)] Hard carbon obtained under argon gas.

The fibrous microstructure of the cellulose is obvious in the SEM images of the HC, even after grinding the samples (Fig. 1). Samples that had been reacted with $TiCl_4$ before pyrolysis had an obvious surface roughening, increasing with the titanium loading and with nanoparticles visible on the surfaces of the fibrous structures, and TEM images confirmed this observation as well as showing crystallite sizes consistent with those listed in Table 1 (Figs. 1, 2 and supplementary information Figs. S2-S4). The images suggest that the surfaces are quite consistent within a particular sample and the corresponding EDX mapping images (Figs. 1 and S4) reveal that the distribution of titanium across the HC structure is very uniform.

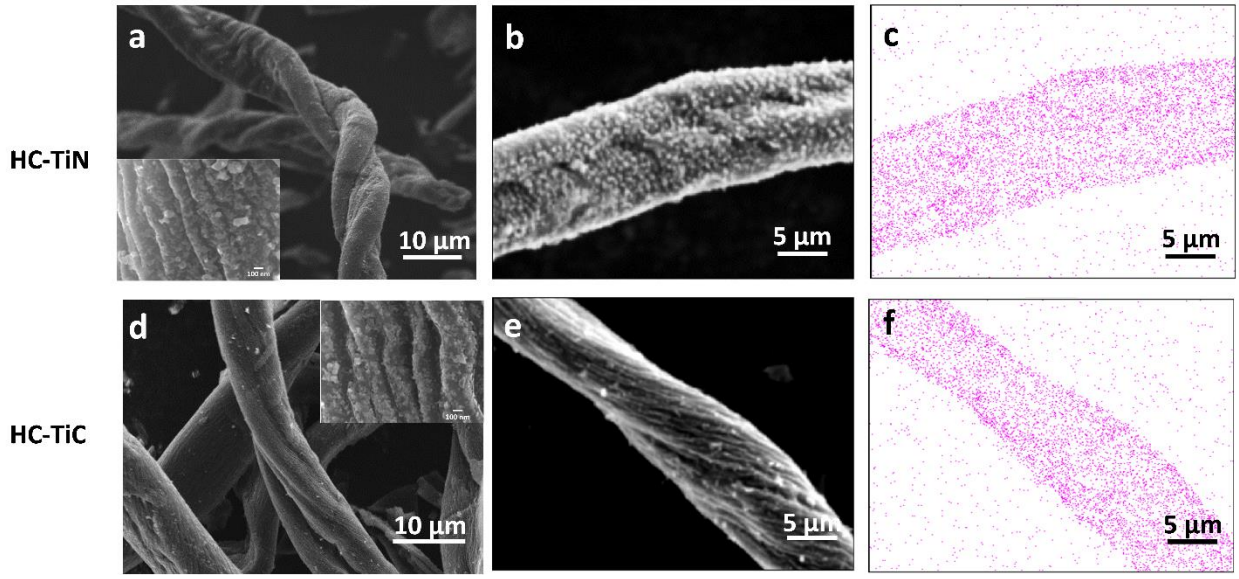

Fig. 1 SEM images of HC-TiN (a and b) and HC-TiC (d and e) composites . The purple dots in the EDX maps (c and f) represent the dispersion of titanium in these samples and are acquired in the same regions as the corresponding SEM images (b and e).

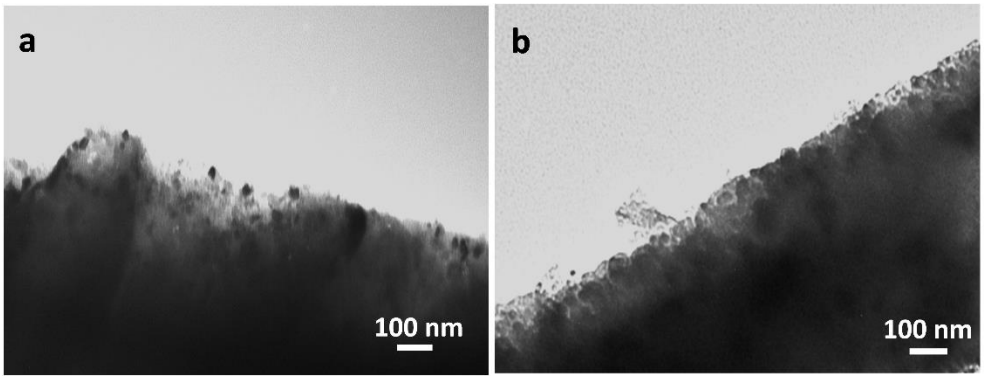

Fig. 2 TEM images of HC-TiN (a) and HC-TiC (b) composites showing crystallites at the surfaces and hard carbon domain features in the body of the fibers.

Fig. 3 displays the XRD patterns of composites with different mass loadings of titanium nitride or carbide. The broad peaks around 23° correspond to the 002 peak of the graphitic domains of the hard carbon[43] (data refinement can be seen in supplementary information, Fig. S5). This peak can be used to calculate the interlayer d-spacing of the hard carbon (Table 1), which was found to increase with titanium loading. A wider interlayer separation has been linked to better sodium ion insertion and deinsertion,[44] and may suggest some limited titanium insertion between the layers. The interlayer spacing of thermally expanded graphite can reach 0.43 nm,[45] and others have observed increased interlayer spacings on introducing aluminium ions into graphite[46], so the increases in interlayer spacing observed here are plausible. A second broad HC feature is also observed around 44°, corresponding to the 100 peak of the graphitic domains.

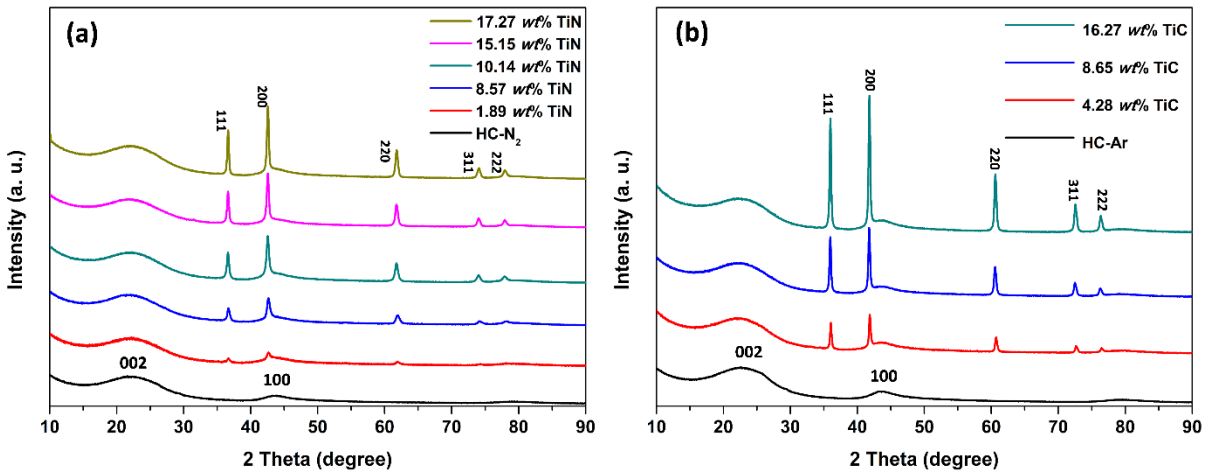

Fig.3 The XRD patterns of HC-TiN (a) and HC-TiC (b) composites, with loadings as shown.

As the titanium loading increased, the sharper peaks increased in intensity. These had the familiar rocksalt-type pattern expected for the cubic TiC, TiN or TiO. The patterns were refined and the extracted lattice parameters are shown in Table 1. In Fig. 4 the lattice parameters are compared with those reported in the Inorganic Crystal Structure Database (ICSD)[47] for the TiC, TiN or TiO phases that were considered to be potential constituents of the composites. It can be seen that the lattice parameter decreases fairly linearly from TiC (~4.32 Å) to TiN (~4.24 Å) and TiO (~4.17 Å), and that the reported lattice parameters for these phases occur in quite narrow bands. The lattice parameters from Table 1 are shown as two bands in Fig. 4, where it is clear that the composites fired in nitrogen all have lattice parameters close to the ICSD values for TiN, and those fired in argon are all close to TiC. These systems are known to form solid solutions and the presence of the other two anions in the samples cannot be ruled out, but this is difficult to measure in the presence of a large excess of carbon. For both composites, the diffraction peaks become narrower as the titanium loading increases, implying that the crystallite sizes become larger. The HC-TiN composites have broader diffraction peaks than the HC-TiC composites with similar $TiCl_4$ concentrations. Crystallite size of TiN varies from 3.6 to 34.0 nm while that of TiC varies from 19.1 to 38.0 nm (Table 1, data fitted in the PDXL package).

The melting points of titanium nitride and titanium carbide are 3228 K (2930 °C) and 3458 K (3160 °C), respectively. Tammann temperatures are typically 50-75% of the melting point and are expected to be above 1614 K and 1729 K, respectively. The synthesis temperature in our experiment is 1698 K (1400 °C). Hence the larger titanium carbide crystallite sizes are not consistent with annealing rates at this firing temperature. On the other hand, the synthesis temperature is 86% of the melting point of titanium (1966 K or 1668 °C), which is a potential intermediate during the synthesis process. After reaction with the oxidic cellulose surface the titanium is likely to be present in a form chemically similar to TiO_2. The high temperature synthesis is likely to involve carbothermal reduction of the titanium-containing species either combined with (equations (1) and (2)), or followed by (equations (3) to (5)), reaction with gaseous nitrogen or further carbon from the HC surface. The larger crystallite sizes of TiC suggest that equations (3)-(5) are important, since if the more sinterable titanium metal is present during the synthesis it could react more

rapidly to make TiN, utilizing gas phase diffusion of nitrogen, than to make TiC by solid state diffusion of carbon.

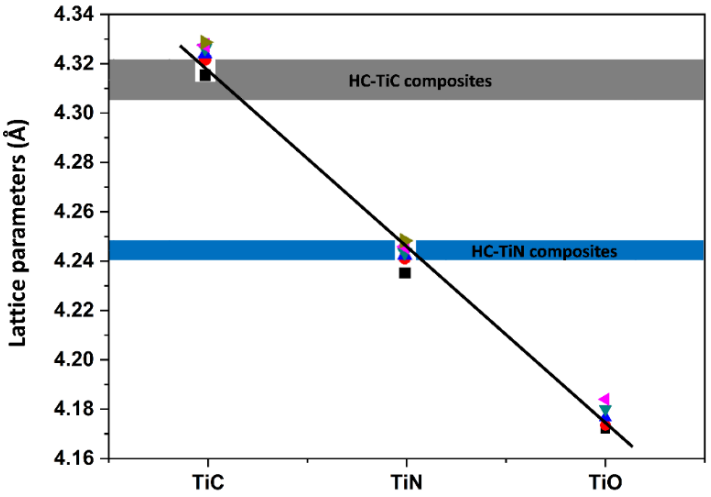

Fig.4 Symbols and best-fit line showing the literature lattice parameters of TiC[48-52], TiN[49, 53-57] and TiO[58-62] from ICSD.[47] The blue and grey banded regions represent the range of lattice parameters found for the components designated as TiN or TiC (Table 1) in the composites obtained in this study.

$$\mathrm{Ti}O_2 + \frac{1}{2}N_2 + 2\mathrm{C} \rightarrow \mathrm{TiN} + 2\mathrm{CO} \quad (1)$$

$$\mathrm{Ti}O_2 + 3\mathrm{C} \rightarrow \mathrm{TiC} + 2\mathrm{CO} \quad (2)$$

$$\mathrm{Ti}O_2 + 2\mathrm{C} \rightarrow \mathrm{Ti} + 2\mathrm{CO} \quad (3)$$

$$\mathrm{Ti} + \frac{1}{2}N_2 \rightarrow \mathrm{TiN} \quad (4)$$

$$\mathrm{Ti} + \mathrm{C} \rightarrow \mathrm{TiC} \quad (5)$$

Raman spectroscopy is particularly useful to investigate the HC component of the composites when the PXRD is dominated by the metal nitrides.[63] In Fig. 5, the Raman plots show broad peaks due to hard carbon around 1310 and 1595 cm^{-1}, which can be attributed to the disordered (D-band) and ordered graphitic (G-band) structures in hard carbon, respectively.[43,64] The spectral analysis by curve fitting is illustrated in supplementary information, Fig. S6. The D and G bands were fitted with Lorentzian functions and a small D3 band contribution (amorphous carbon, 1500 cm^{-1}) as a Gaussian function as described by others.[65] The integrated intensity of the D-band is stronger than that of G-band, suggesting that the composites retain the highly disordered graphitic structure of hard carbon. The integrated intensity ratio I_D/I_G goes up from 1.71 to 2.03 (Table 1) with increasing titanium loading in HC-TiN composites, and from 1.58 to 2.16 (Table 1) with increasing titanium in HC-TiC. This suggests that the presence of TiN or TiC in the composites increases disorder, in accordance previous reports of introducing metallic atoms to an amorphous substrate.[66,67] There are no obvious strong peaks between 300 and 600 cm^{-1}, where the presence of any titanium dioxide would be expected to produce strong peaks (supplementary information, Fig. S7).[63]

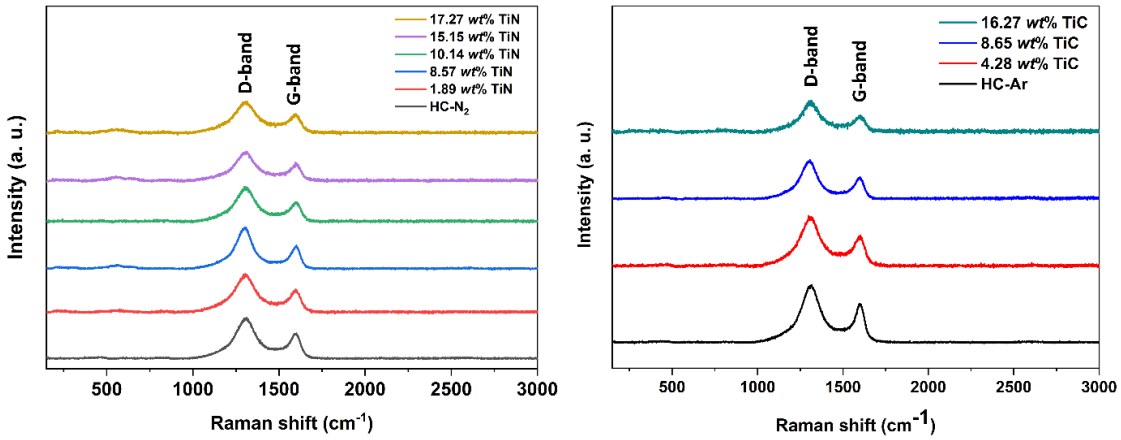

Fig. 5 Raman spectra of HC-TiN (a) and HC-TiC (b) composites with titanium loadings as marked.

XPS spectra of the HC-TiN and HC-TiC composites are shown in Fig. 6 and peak attributions from the C 1s, O 1s, N 1s and Ti 2p core-level regions are collected in Table 2. The measured atomic concentration of C: N: O: Ti is 83.4: 4.7: 7.9: 4.0 in HC-TiN composite, while that of C: O: Ti is 92.5: 5.1: 2.4 in HC-TiC composite, both reflecting surface oxidation of the composites, which were handled in air before loading into the instrument.[71,74] The survey spectra of both composites and XPS data for the non-loaded HC samples can be seen in the supporting information (Fig. S8 and S9). The C 1s deconvolution spectra show binding energies of 284.5 and 284.6 eV, respectively, which are typical of sp^2 carbon.[68] The peaks with higher binding energy can be attributed to sp^3 C, C-O, C=O, and π-π^* shake-up satellites.[44,68] The high peak intensity ratio of sp^2/sp^3 suggests high levels of structural defects in the hard carbon[69], corroborating the above Raman discussion. The obvious peak at lower binding energy of 281.8 eV in HC-TiC is associated with TiC and the smaller shoulder at 283.0 eV corresponds to titanium subcarbide.[70] The Ti $2p_{3/2}$ feature at 455.1 eV in HC-TiC also shows the presence of TiC. The peak at 455.4 eV corresponds to TiN in HC-TiN composite, while the peak at higher binding energy of 456.4 eV can be assigned to Ti-O-N, due to charge transfer from Ti to O that causes the chemical state shift toward to higher binding energy.[71-73] The peaks at 458.5 and 458.7 eV correspond to the surface oxide from HC-TiN and HC-TiC, respectively. In addition to the O 1s peak at 530.1 eV, attributable to surface oxidation of the Ti component of the composites, two peaks with higher binding energy are from absorbed carbonyl groups,[75] which is consistent with the discussion of the C 1s region. The peak at 397.4 eV in the N 1s spectrum indicates stoichiometric TiN.[61] The peak appears at a lower binding energy of 396.3 eV corresponds to oxynitride species, which is consistent with the Ti-O-N components in Ti 2p analysis. The components at 398.5 and 401.1 eV can be related to oxygen species and free molecular N_2 on the surface of TiN, respectively.[74] The N 1s spectrum in Fig. S9 shows a small nitrogen component (0.1 % atom concentration) in HC-N_2, and the spectrum fitting is good without the presence of C-N in HC-TiN, suggesting no obvious evidence of nitrogen doping in hard carbon or in HC-TiN composite. Some XPS studies of thin film samples use Ar^+ etching before measurement to remove oxide,[76,77] but this is less effective on complex morphologies as studied here (the XRD and Raman do suggest the oxide is thin). The XPS data confirm the presence of TiN and TiC on the carbon surfaces, consistent with the XRD and Raman analysis.

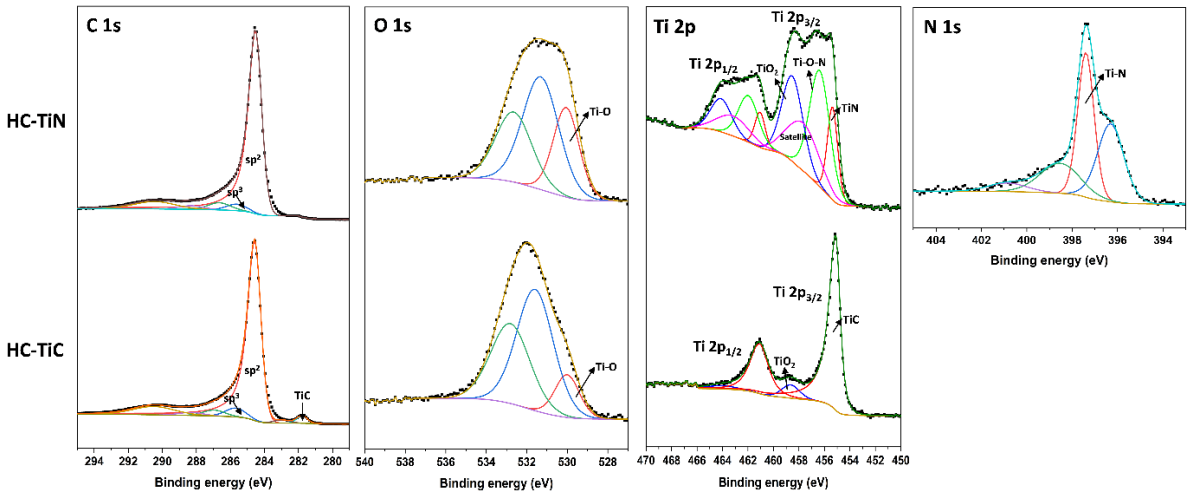

Fig. 6 High resolution XPS spectra of the C 1s, O 1s, N 1s and Ti 2p regions for HC-TiN and HC-TiC composites with 15.15 *wt*% TiN and 8.65 *wt*% TiC, respectively.

Table 2 C 1s, O 1s, N 1s and Ti 2p core-level XPS peaks with likely chemical states

Material	C 1s		O 1s		Ti $2p_{3/2}$		N 1s	
	BE (eV)	State	BE (eV)	State	BE (eV)	State	BE (eV)	State
HC-TiN	284.5	C-C, sp^2	530.1	O-Ti	455.4	Ti-N	396.3	N-O-Ti
	285.6	C-C, sp^3	531.3	O=C	456.4	Ti-O-N	397.4	N-Ti
	286.7	C-O	532.6	O-C	457.7	Satellite	398.6	N-O
	288.3	C=O			458.5	TiO_2	400.99	N_2
	290.4	Satellite						
HC-TiC	281.8	C-Ti	530.1	O-Ti	455.1	Ti-C		
	283.0	subcarbide	531.6	O=C	458.8	TiO_2		
	284.6	C-C, sp^2	532.8	O-C				
	285.7	C-C, sp^3						
	286.9	C-O						
	288.3	C=O						
	290.5	Satellite						

N_2 adsorption and desorption isotherms of the HC-TiN and HC-TiC composites are shown in Fig. 7. All can be classified as type IV with H4 hysteresis, implying that the materials possess mesoporosity.[78] A feature common to these hysteresis loops is that complete closure points should appear at nitrogen's boiling point around P/P_0 = 0.42. However, for some materials containing micropores, low pressure hysteresis can be extended to the lowest attainable pressures as seen in these isotherms.[79-81] The pore size distribution (supplementary information, Fig. S10) shows a range of sizes from below 2 nm to around 14 nm. At low concentration of $TiCl_4$, the specific surface area (Table 1) of the composites increases when compared with the pure hard carbon. That may be because of particles forming on the surface or the reaction between

the titanium chloride and the cellulose may roughen the surface. Further increases in titanium loading increase the TiN or TiC particle size, and then the surface area does not increase further (HC-TiN) or decreases (HC-TiC). The reduced surface area may also be due to covering or filling of micropores near the surface of the HC.

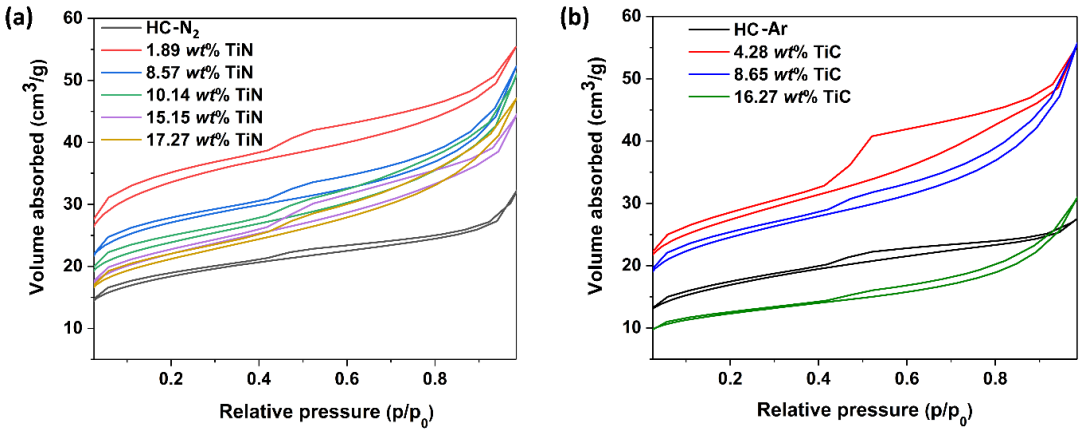

Fig. 7 N_2 adsorption and desorption profile of HC-TiN (a) and HC-TiC (b), with loadings as shown.

The viability of the composites for sodium-ion battery applications was tested in sodium half cells with a 1 mol dm^{-3} $NaClO_4$ in 1:1 EC/DEC electrolyte. Fig. 8a shows the first cycle of charge-discharge profiles of the pure HC fired in N_2 and HC-TiN composites and Fig. S11 shows the differential capacity plot, emphasizing that the bulk of the charge is passed around 0.1 V vs Na/Na^+. The pure hard carbon has the highest first cycle specific capacity of 290.7 mA h g^{-1} at current of 50 mA g^{-1}, which is competitive with the capacities of other hard carbons obtained from various biomass sources. For example, Hu[82] reported leaf-based carbon and the charge capacity is 270 mA h g^{-1} at 40 mA g^{-1}. Xu[83] obtained nitrogen-rich hard carbon by the pyrolysis of shrimp skin with the capacity of 276 mA h g^{-1} at a current of 100 mA g^{-1}. Ding[38] synthesized hard carbon from peat moss with capacity of 298 mA h g^{-1} at current 50 mA g^{-1}.

The capacities of the HC-TiN composites were all similar to 290.7 mA h g^{-1}. (280.6 mA h g^{-1} at 1.89 *wt*%; 273.3 mA h g^{-1} at 8.57 *wt*%; 271.4 mA h g^{-1} at 10.14 *wt*%; 283.4 mA h g^{-1} at 15.15 *wt*%; 261.1 mA h g^{-1} at 17.27 *wt*%). The low first cycle Coulombic efficiency of pure HC (68.4% efficiency) is mainly caused by the formation of the solid electrolyte interface (SEI), which is proportional to the surface area of HC exposed to the electrolyte.[84] The measured BET surface area of 15.15 *wt*% HC-TiN composite is 73 m^2 g^{-1}, which may explain its slightly lower first cycle Coulombic efficiency (66.8%), and utilization of this material might require pre-sodiation. The 15.15 *wt*% HC-TiN composite continued to have similar capacities to those of HC over the first 20 charge/discharge cycles, but then as the capacity of HC drops the composite exhibits a better capacity retention (Fig. 8b, with a repeat data set in supplementary information, Fig. S12). At the 50^{th} cycle, the HC-TiN composite had a Coulombic efficiency of 99.5% and reversible capacity of 241.5 mA h g^{-1}, 85.2% of its initial capacity. The HC had a 50^{th} cycle capacity of 215.9 mA h g^{-1}, retaining 74.3% of its initial value. Electrochemical impedance spectroscopy (Fig. 9) shows that the HC and 15.15 *wt*% HC-TiN composite have similar charge transfer resistances (R_{ct}) initially, but that after 50 cycles the HC had

become more resistive (R_{ct}=296 Ω) than the composite (R_{ct}=105 Ω), suggesting that the highly conductive TiN on the surface plays a role to improve the charge transfer kinetics.

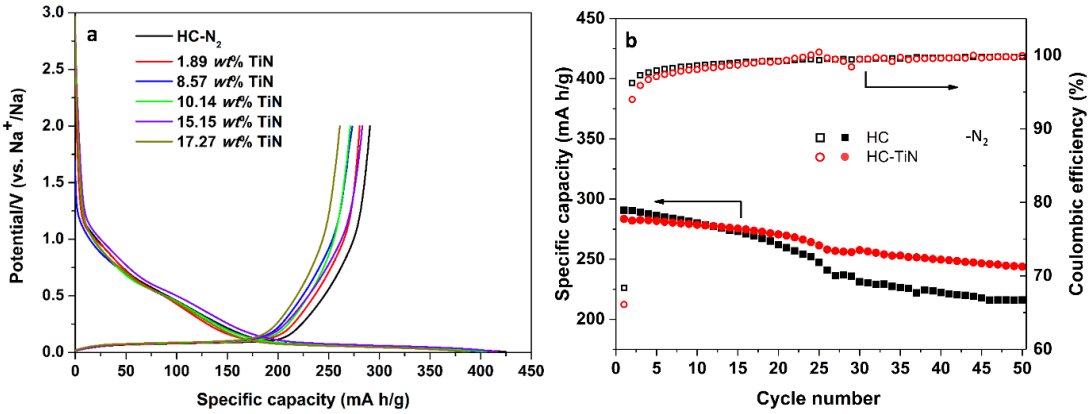

Fig. 8 The first cycle charge-discharge profiles of HC-N_2 and HC-TiN compositions as shown (a) and cycling performance of HC-N_2 and the 15.15 *wt*% HC-TiN composite (b) between 2.0 and 0.005 V (vs. Na^+/Na) at 50 mA g^{-1}.

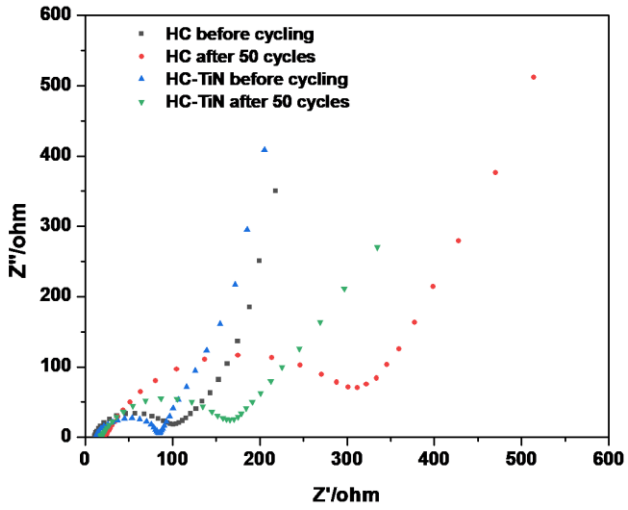

Fig. 9 Nyquist plots of HC and 15.15 *wt*% HC-TiN composites before and after 50 cycles between 2.0 and 0.005 V vs. Na^+/Na at 50 mA g^{-1}.

Ex situ grazing incidence XRD patterns of the HC-TiN composites removed from cells at various stages of cycling (Fig. 10) showed Cu from the backing foil and TiN. The TiN particle size decreases from 14.7 to 11.2 nm (supplementary information, Table. S1) after first reduction process. In the tenth cycle, the particle size almost has no change in the reduced or oxidized electrode, which may be due to reactions occurring only on the surface of TiN. Refinements of the data (supplementary information, Fig. S13) showed no change in the lattice parameter comparing the reduced *vs* oxidized materials or comparing the materials after 1 *vs* 10 cycles (Table 3). A previous study showed that titanium nitride can be reduced to the metal in lithium batteries,[85] but its storage mechanism in sodium batteries is not clear. Research in our group[10-

[13] has shown that in several cases only the surface of metal nitrides reacts, and the small variations seen here suggest that TiN has only reacted in the surface region during cycling *vs* sodium.

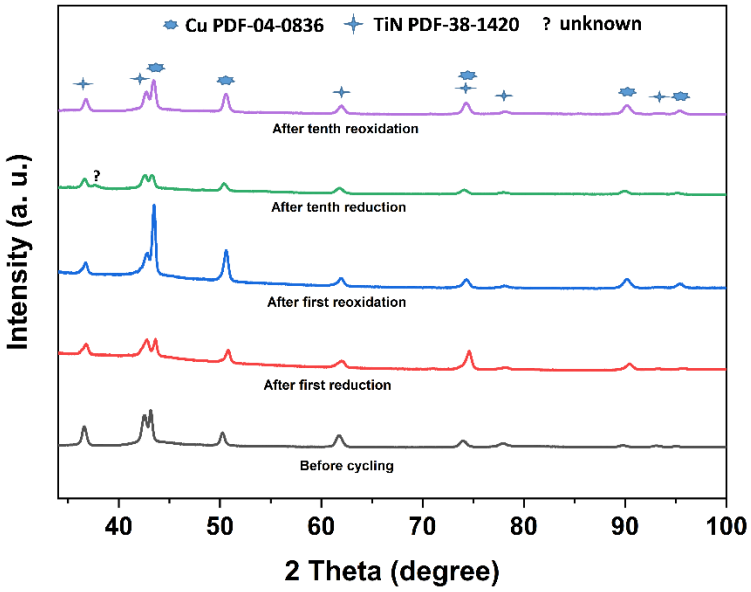

Fig. 10 *Ex situ* grazing incidence XRD patterns of HC-TiN composite-based electrodes at various stages of cycling when reducing to 5 mV and oxidizing back to 2 V vs. Na^+/Na.

Table 3 Lattice parameters of TiN in the composites before cycling and after different cycling times.

Galvanostatic cycling stage at which sample was removed from cell	TiN		
	Lattice parameter (Å)	R_{wp} (%)	R_p (%)
Before cycling	4.24476(19)	2.9	2.1
After first reduction	4.24215(15)	3.5	2.8
After first oxidation	4.2439(3)	3.3	2.4
After tenth reduction	4.2416(2)	2.9	2.3
After tenth oxidation	4.23701(13)	3.2	2.5

Galvanostatic cycling of the HC-TiC composite electrodes (Fig.11a) showed the 8.65 *wt*% HC-TiC composite electrode to have the best capacity (280.8 mA h g^{-1}), again a little lower than the pure HC fired in Ar (284.5 mA h g^{-1}). The capacity of the other composites was 263.7 mA h g^{-1} in 4.28 *wt*% HC-TiC and 247.8 mA h g^{-1} in 16.27 *wt*% HC-TiC. Previous studies show TiC can be used to increase the conductivity of composite electrodes,[86,87] thus enhancing the capacity. This is not observed here, the TiC composites produce slightly lower capacities and, unlike TiN, do not improve the cycling behavior (Fig. 11b). The larger TiC crystallite size of TiC in HC-TiC composite may reduce its ability to participate in reactions, or the TiC surfaces may be less reactive than the TiN. The coulombic efficiency of the 8.65 *wt*% HC-TiC composite was 99.6% after

50 cycles, while the capacity decreased from 280.8 to 186.8 mA h g^{-1} after 50 cycles, a capacity retention of 66.5%.

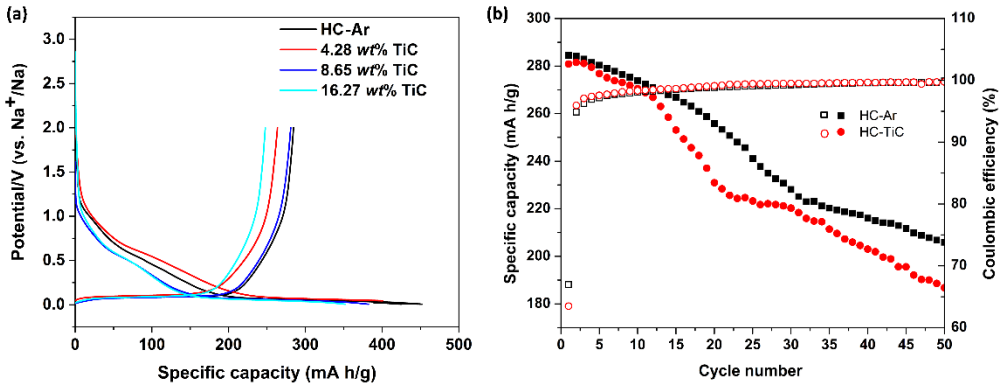

Fig. 11 (a) Charge-discharge profiles of HC-Ar and HC-TiC composites electrodes between 2.0 and 0.005 V (vs. Na^+/Na) at 50 mA/g, (b) cyclic performance of HC-TiC composites in 50 cycles.

The HC-TiN composites prepared by the new methodology presented above have some promise in SIBs and the method is applicable to depositing other metal nitrides or carbides on the carbon surfaces. This could be for batteries, but the literature[19,88]also suggests that such carbon-metal nitride/carbide composites could be applied in electrocatalysis and supercapacitors.

CONCLUSIONS

Reactions of titanium tetrachloride with cellulose followed by carbothermal nitridation or reduction during firing produce hard carbon with nanocrystalline titanium nitride or carbide decorated over the surfaces. In sodium cells both composites show similar first cycle capacities to hard carbon, but the titanium nitride composite delivers a better capacity retention (85.2%) after 50 cycles than that of hard carbon (74.3 %). Moreover, we expect the synthesis method demonstrated here will provide an effective way to obtain composites with other metal nitrides and carbides for sodium cell and other energy applications.

ASSOCIATED CONTENT

The Supporting Information contains SEM images of HC-TiN and HC-TiC composites, TGA analysis, XPS survey, C 1s and O 1s core-level spectra of HC-Ar and HC-N_2, and pore size distribution of HC-TiN and HC-TiC composites.

AUTHOR INFORMATION

Corresponding Author

*Email: A.L.Hector@soton.ac.uk

Notes

The authors declare no competing financial interest.

ACKNOWLEDGMENTS

HC thanks the China Scholarship Council (CSC) and the University of Southampton for support. NGA thanks the EPSRC for an early career fellowship (EP/N024303/1) and SS is funded under EP/N035437/1. We would like to acknowledge Dr. Shaoliang Guan and Harwell XPS, the EPSRC National Facility for X-Ray Photoelectron Spectroscopy for collection of the XPS data. We wish to acknowledge the use of the EPSRC funded National Chemical Database Service hosted by the Royal Society of Chemistry.

REFERENCES

(1) Chen, J. G. Carbide and Nitride Overlayers on Early Transition Metal Surfaces: Preparation, Characterization, and Reactivities. *Chem. Rev.* **1996**, *96*, 1477-1498.

(2) Glatzel, S.; Schnepp, Z.; Giordano, C. From Paper to Structured Carbon Electrodes by Inkjet Printing. *Angew. Chem. Int. Ed.* **2013**, *52*, 2355-2358.

(3) Xia, D.; Liu, S.; Wang, Z.; Chen, G.; Zhang, L.; Zhang, L.; Hui, S.; Zhang, J. Methanol-tolerant MoN Electrocatalyst Synthesized Through Heat Treatment of Molybdenum Tetraphenylporphyrin for Four-electron Oxygen Reduction Reaction. *J. Power Sources* **2008**, *177*, 296-302.

(4) Chhina, H.; Campbell, S.; Kesler, O. Thermal and Electrochemical Stability of Tungsten Carbide Catalyst Supports. *J. Power Sources* **2007**, *164*, 431-440.

(5) Choi, D.; Blomgren, G. E.; Kumta, P. N. Fast and Reversible Surface Redox Reaction in Nanocrystalline Vanadium Nitride Supercapacitors. *Adv. Mater.* **2006**, *18*, 1178-1182.

(6) Zhong, Y.; Xia, X.; Zhan, J.; Wang, Y.; Wang, X.; Tu, J. Monolayer Titanium Carbide Hollow Sphere Arrays Formed via an Atomic Layer Deposition Assisted Method and Their Excellent High-temperature Supercapacitor Performance. *J. Mater. Chem. A* **2016**, *4*, 18717-18722.

(7) Pereira, N.; Dupont, L.; Tarascon, J. M.; Klein, L. C.; Amatucci, G. G. Electrochemistry of Cu_3N with Lithium. *J. Electrochem. Soc.* **2003**, *150*, A1273.

(8) Fu, Z.-W.; Wang, Y.; Yue, X.-L.; Zhao, S.-L.; Qin, Q.-Z. Electrochemical Reactions of Lithium with Transition Metal Nitride Electrodes. *J. Phys. Chem. B* **2004**, *108*, 2236-2244.

(9) Sun, Q.; Dai, Y.; Ma, Y.; Jing, T.; Wei, W.; Huang, B. Ab Initio Prediction and Characterization of Mo_2C Monolayer as Anodes for Lithium-Ion and Sodium-Ion Batteries. *J. Phys. Chem. Lett.* **2016**, *7*, 937-943.

(10) Li, X.; Hasan, M. M.; Hector, A. L.; Owen, J. R. Performance of nanocrystalline Ni3N as a negative electrode for sodium-ion batteries. *J. Mater. Chem. A* **2013**, *1*, 6441.

(11) Li, X.; Hector, A. L.; Owen, J. R.; Shah, S. I. U. Evaluation of Nanocrystalline Sn_3N_4 Derived from Ammonolysis of $Sn(NEt_2)_4$ as a Negative Electrode Material for Li-ion and Na-ion Batteries. *J. Mater. Chem. A* **2016**, *4*, 5081-5087.

(12) Shah, S. I. U.; Hector, A. L.; Li, X.; Owen, J. R. Solvothermal synthesis and electrochemical charge storage assessment of Mn3N2. *J. Mater. Chem. A* **2015**, *3*, 3612-3619.

(13) Li, X.; Hector, A. L.; Owen, J. R. Evaluation of Cu3N and CuO as Negative Electrode Materials for Sodium Batteries. *J. Phys. Chem. C* **2014**, *118*, 29568-29573.

(14) Cui, Z.; Li, C.; Yu, P.; Yang, M.; Guo, X.; Yin, C. Reaction Pathway and Wiring Network Dependent Li/Na Storage of Micro-sized Conversion Anode with Mesoporosity and Metallic Conductivity. *J. Mater. Chem. A* **2015**, *3*, 509-514.

(15) Lv, X.; Song, J.; Lai, Y.; Fang, J.; Li, J.; Zhang, Z. Ultrafine Nanoparticles Assembled Mo_2C Nanoplates as Promising Anode Materials for Sodium Ion Batteries with Excellent Performance. *J. Energy Storage* **2016**, *8*, 205-211.

(16) Biener, J.; Stadermann, M.; Suss, M.; Worsley, M. A.; Biener, M. M.; Rose, K. A.; Baumann, T. F. Advanced Carbon Aerogels for Energy Applications. *Energy Environ. Sci.* **2011**, *4*, 656.

(17) Zou, G.; Hou, H.; Foster, C. W.; Banks, C. E.; Guo, T.; Jiang, Y.; Zhang, Y.; Ji, X. Advanced Hierarchical Vesicular Carbon Co-Doped with S, P, N for High-Rate Sodium Storage. *Adv. Sci.* **2018**, *5*, 1800241.

(18) Peng, S.; Li, L.; Kong Yoong Lee, J.; Tian, L.; Srinivasan, M.; Adams, S.; Ramakrishna, S. Electrospun Carbon Nanofibers and Their Hybrid Composites as Advanced Materials for Energy Conversion and Storage. *Nano Energy* **2016**, *22*, 361-395.

(19) Park, J.; Jun, Y.-S.; Lee, W.-r.; Gerbec, J. A.; See, K. A.; Stucky, G. D. Bimodal Mesoporous Titanium Nitride/Carbon Microfibers as Efficient and Stable Electrocatalysts for Li–O_2 Batteries. *Chem. Mater.* **2013**, *25*, 3779-3781.

(20) Yousef, A.; Brooks, R. M.; El-Newehy, M. H.; Al-Deyab, S. S.; Kim, H. Y. Electrospun Co-TiC Nanoparticles Embedded on Carbon Nanofibers: Active and Chemically Stable Counter Electrode for Methanol Fuel Cells and Dye-sensitized Solar Cells. *Int. J. Hydrogen Energy* **2017**, *42*, 10407-10415.

(21) Wu, Z.-S.; Ren, W.; Wen, L.; Gao, L.; Zhao, J.; Chen, Z.; Zhou, G.; Li, F.; Cheng, H.-M. Graphene Anchored with Co_3O_4 Nanoparticles as Anode of Lithium Ion Batteries with Enhanced Reversible Capacity and Cyclic Performance. *ACS Nano* **2010**, *4*, 3187-3194.

(22) Liao, H.; Hou, H.; Zhang, Y.; Qiu, X.; Ji, X. Nano-confined Mo_2C Particles Embedded in a Porous Carbon Matrix: A Promising Anode for Ultra-stable Na Storage. *ChemElectroChem* **2017**, *4*, 2669-2676.

(23) Zhu, Y.; Chen, G.; Xu, X.; Yang, G.; Liu, M.; Shao, Z. Enhancing Electrocatalytic Activity for Hydrogen Evolution by Strongly Coupled Molybdenum Nitride@Nitrogen-Doped Carbon Porous Nano-Octahedrons. *ACS Catalysis* **2017**, *7*, 3540-3547.

(24) Zhang, J.; Hector, A. L.; Soulé, S.; Zhang, Q.; Zhao, X. Effects of Ammonolysis and of Sol–gel Titanium Oxide Nitride Coating on Carbon Fibres for Use in Flexible Supercapacitors. *J. Mater. Chem. A* **2018**, *6*, 5208-5216.

(25) Gao, Q.; Zhao, X.; Xiao, Y.; Zhao, D.; Cao, M. A Mild Route to Mesoporous Mo_2C-C Hybrid Nanospheres for High Performance Lithium-ion Batteries. *Nanoscale* **2014**, *6*, 6151-6157.

(26) Nagelberg, A. S.; Worrell, W. L. A Thermodynamic Study of Sodium-intercalated Tantalum(IV) and Titanium(IV) Sulfides. *J. Solid State Chem.* **1979**, *29*, 345-354.

(27) Parant, J.-P.; Olazcuaga, R.; Devalette, M.; Fouassier, C.; Hagenmuller, P. Sur Quelques Nouvelles Phases de Formule Na_xMnO_2 ($x \leqslant 1$). *J. Solid State Chem.* **1971**, *3*, 1-11.

(28) Braconnier, J. J.; Delmas, C.; Fouassier, C.; Hagenmuller, P. Electrochemical Behavior of the Sodium Cobalt Oxide (Na_xCoO_2) Phases. *Mater. Res. Bull.* **1980**, *15*, 1797-1804.

(29) Slater, M. D.; Kim, D.; Lee, E.; Johnson, C. S. Sodium-Ion Batteries. *Adv. Funct. Mater.* **2013**, *23*, 947-958.

(30) Luo, W.; Shen, F.; Bommier, C.; Zhu, H.; Ji, X.; Hu, L. Na-Ion Battery Anodes: Materials and Electrochemistry. *Acc. Chem. Res.* **2016**, *49*, 231-240.

(31) Hwang, J. Y.; Myung, S. T.; Sun, Y. K. Sodium-ion batteries: present and future. *Chem. Soc. Rev.* **2017**, *46*, 3529-3614.

(32) Web of Science Database Search, Thompson-Reuters. **2018**.

(33) Jache, B.; Adelhelm, P. Use of graphite as a highly reversible electrode with superior cycle life for sodium-ion batteries by making use of co-intercalation phenomena. *Angew. Chem. Int. Ed.* **2014**, *53*, 10169-10173.

(34) Luo, W.; Bommier, C.; Jian, Z.; Li, X.; Carter, R.; Vail, S.; Lu, Y.; Lee, J. J.; Ji, X. Low-surface-area hard carbon anode for na-ion batteries via graphene oxide as a dehydration agent. *ACS Appl. Mater. Interfaces* **2015**, *7*, 2626-2631.

(35) Muñoz-Márquez, M. Á.; Saurel, D.; Gómez-Cámer, J. L.; Casas-Cabanas, M.; Castillo-Martínez, E.; Rojo, T. Na-Ion Batteries for Large Scale Applications: A Review on Anode Materials and Solid Electrolyte Interphase Formation. *Adv. Energy Mater.* **2017**, *7*, 1700463.

(36) Hasegawa, G.; Kanamori, K.; Kannari, N.; Ozaki, J.-i.; Nakanishi, K.; Abe, T. Hard Carbon Anodes for Na-Ion Batteries: Toward a Practical Use. *ChemElectroChem* **2015**, *2*, 1917-1920.

(37) Tang, K.; Fu, L.; White, R. J.; Yu, L.; Titirici, M.-M.; Antonietti, M.; Maier, J. Hollow Carbon Nanospheres with Superior Rate Capability for Sodium-based Batteries. *Adv. Energy Mater.* **2012**, *2*, 873-877.

(38) Ding, J.; Wang, H.; Li, Z.; Kohandehghan, A.; Cui, K.; Xu, Z.; Zahiri, B.; Tan, X.; Lotfabad, E. M.; Olsen, B. C.; Mitlin, D. Carbon Nanosheet Frameworks Derived from Peat Moss as High Performance Sodium Ion Battery Anodes. *ACS Nano* **2013**, *7*, 11004-11015.

(39) Peled, E.; Eshkenazi, V.; Rosenberg, Y. Study of Lithium Insertion in Hard Carbon Made from Cotton Wool. *J. Power Sources* **1998**, *76*, 153-158.

(40) Toby, B. H. EXPGUI, A Graphical User Interface for GSAS. *J. Appl. Crystallogr.* **2001**, *34*, 210-213.

(41) Shirley, D. A. High-resolution X-ray Photoemission Spectrum of the Valence Bands of Gold. *Phys. Rev. B* **1972**, *[3]5*, 4709-4714.

(42) Hon, D. N. S.; Editor: *Chemical Modification of Lignocellulosic Materials*; Dekker, 1996. pp. 2-3.

(43) Zhou, H. C.; Long, J. R.; Yaghi, O. M. Introduction to metal-organic frameworks. *Chemical reviews* **2012**, *112*, 673-674.

(44) Yu, Z.-L.; Xin, S.; You, Y.; Yu, L.; Lin, Y.; Xu, D.-W.; Qiao, C.; Huang, Z.-H.; Yang, N.; Yu, S.-H.; Goodenough, J. B. Ion-catalyzed Synthesis of Microporous Hard Carbon Embedded with Expanded Nanographite for Enhanced Lithium/Sodium Storage. *J. Am. Chem. Soc.* **2016**, *138*, 14915-14922.

(45) Wen, Y.; He, K.; Zhu, Y.; Han, F.; Xu, Y.; Matsuda, I.; Ishii, Y.; Cumings, J.; Wang, C. Expanded graphite as superior anode for sodium-ion batteries. *Nat. Commun.* **2014**, *5*, 4033.

(46) Yu, W.; Yu, T.; Graham, N. Development of a stable cation modified graphene oxide membrane for water treatment. *2D Materials* **2017**, *4*, 045006.

(47) <1.pdf>.

(48) Elliott, R. O.; Kempter, C. P. Thermal Expansion of Some Transition Metal Carbides. *J. Phys. Chem.* **1958**, *62*, 630-631.

(49) Pessall, N.; Gold, R. E.; Johansen, H. A. Superconductivity in Interstitial Compounds. *J. Phys. Chem. Solids* **1968**, *29*, 19-38.

(50) Stuart, H.; Ridley, N. Thermal Expansion of Some Carbides and Tessellated Stresses in Steels. *J. Iron Steel Inst.* **1970**, *208*, 1087-1092.

(51) Kieffer, R.; Nowotny, H.; Ettmayer, P.; Dufek, G. Miscibility of Transition Metal Nitrides and Carbides. *Metall* **1972**, *26*, 701-708.

(52) Rogl, P.; Naik, S. K.; Rudy, E. A Constitutional Diagram of the System Titanium Carbide-hafnium Carbide-tungsten Carbide. *Monatsh. Chem.* **1977**, *108*, 1189-1211.

(53) Bannister, F. A. Osbornite, Meteoritic Titanium Nitride. *Mineral. Mag. J. Mineral. Soc.* **1941**, *26*, 36-44.

(54) Duwez, P.; Odell, F. Phase Relationships in the Binary Systems of Nitrides and Carbides of Zirconium, Niobium, Titanium, and Vanadium. *J. Electrochem. Soc.* **1950**, *97*, 299-304.

(55) Nowotny, H.; Benesovsky, F.; Rudy, E. High-melting Systems of Hafnium Carbide and Hafnium Nitride. *Monatsh. Chem.* **1960**, *91*, 348-356.

(56) Gatterer, J.; Dufek, G.; Ettmayer, P.; Kieffer, R. Cubic Tantalum Mononitride (B1) and Its Miscibility with the Transition Metal Nitrides and Carbide isotypes. *Monatsh. Chem.* **1975**, *106*, 1137-1147.

(57) Hasegawa, M.; Yagi, T. Systematic Study of Formation and Crystal Structure of 3d-transition Metal Nitrides Synthesized in a Supercritical Nitrogen Fluid under 10 GPa and 1800 K Using Diamond Anvil Cell and YAG Laser Heating. *J. Alloys Compd.* **2005**, *403*, 131-142.

(58) Rostoker, W. Observations on the Lattice Parameters of the α and TiO Phases in the Titanium-oxygen System. *J. Met.* **1952**, *4*, 981-982.

(59) Straumanis, M. E. Absorption Correction in Precision Determination of Lattice Parameters. *J. Appl. Phys*. **1959**, *30*, 1965-1969.

(60) Hilti, E. New Phases in the Titanium-oxygen System. *Naturwissenschaften* **1968**, *55*, 130-131.

(61) Banus, M. D.; Reed, T. B.; Strauss, A. J. Electrical and Magnetic Properties of TiO and VO. *Phys. Rev. B* **1972**, *5*, 2775-2784.

(62) Taylor, D. Thermal Expansion Data: 1. Binary Oxides with the Sodium Chloride and Wurtzite Structures, MO. *Trans. J. Br. Ceram. Soc.* **1984**, *83*, 5.

(63) Fechler, N.; Fellinger, T.-P.; Antonietti, M. Template-free One-pot Synthesis of Porous Binary and Ternary Metal Nitride@N-doped Carbon Composites from Ionic Liquids. *Chem. Mater.* **2012**, *24*, 713-719.

(64) Sadezky, A.; Muckenhuber, H.; Grothe, H.; Niessner, R.; Poeschl, U. Raman Microspectroscopy of Soot and Related Carbonaceous Materials. Spectral Analysis and Structural Information. *Carbon* **2005**, *43*, 1731-1742.

(65) Kim, J. D.; Roh, J. S.; Kim, M. S. Effect of Carbonization Temperature on Crystalline Structure and Properties of Isotropic Pitch-based Carbon Fiber. *Carbon Lett.* **2017**, *21*, 51-60.

(66) Matenoglou, G. M.; Zoubos, H.; Lotsari, A.; Lekka, C. E.; Komninou, P.; Dimitrakopulos, G. P.; Kosmidis, C.; Evangelakis, G. A.; Patsalas, P. Metal-containing Amorphous Carbon (a-C:Ag) and AlN (AlN:Ag) Metallo-dielectric Nanocomposites. *Thin Solid Films* **2009**, *518*, 1508-1511.

(67) Tembre, A.; Henocque, J.; Clin, M. Infrared and Raman Spectroscopic Study of Carbon-cobalt Composites. *Int. J. Spectrosc.* **2011**, *2011*, 186471, 186476 pp.

(68) Leiro, J. A.; Heinonen, M. H.; Laiho, T.; Batirev, I. G. Core-level XPS Spectra of Fullerene, Highly Oriented Pyrolitic Graphite, and Glassy Carbon. *J. Electron Spectrosc.* **2003**, *128*, 205-213.

(69) Lee, D. W.; Seo, J. W. sp2/sp3 Carbon Ratio in Graphite Oxide with Different Preparation Times. *J. Phys. Chem. C* **2011**, *115*, 2705-2708.

(70) Luthin, J.; Linsmeier, C. Characterization of Electron Beam Evaporated Carbon Films and Compound Formation on Titanium and Silicon. *Phys. Scr., T* **2001**, *T91*, 134-137.

(71) Didziulis, S. V.; Frantz, P.; Perry, S. S.; El-Bjeirami, O.; Imaduddin, S.; Merrill, P. B. Substrate-dependent Reactivity of Water on Metal Carbide Surfaces. *J. Phys. Chem. B* **1999**, *103*, 11129-11140.

(72) Esaka, F.; Furuya, K.; Shimada, H.; Imamura, M.; Matsubayashi, N.; Sato, H.; Nishijima, A.; Kawana, A.; Ichimura, H.; Kikuchi, T. Comparison of Surface Oxidation of Titanium Nitride and Chromium Nitride Films Studied by x-ray Absorption and Photoelectron Spectroscopy. *J. Vac. Sci. Tech.* **1997**, *15*, 2521-2528.

(73) Heide, N.; Siemensmeyer, B.; Schultze, J. W. Surface Characterization and Electrochemical Behavior of Nitrogen- and Carbon-implanted Titanium. *Surf. Interface Anal.* **1992**, *19*, 423-429.

(74) Milosev, I.; Strehblow, H. H.; Navinsek, B.; Metikos-Hukovic, M. Electrochemical and Thermal Oxidation of TiN Coatings Studied by XPS. *Surf. Interface Anal.* **1995**, *23*, 529-539.

(75) Gaddam, R. R.; Jiang, E.; Amiralian, N.; Annamalai, P. K.; Martin, D. J.; Kumar, N. A.; Zhao, X. S. Spinifex nanocellulose derived hard carbon anodes for high-performance sodium-ion batteries. *Sustainable Energy & Fuels* **2017**, *1*, 1090-1097.

(76) Biesinger, M. C.; Lau, L. W. M.; Gerson, A. R.; Smart, R. S. C. Resolving Surface Chemical States in XPS Analysis of First Row Transition Metals, Oxides and Hydroxides: Sc, Ti, V, Cu and Zn. *Appl. Surf. Sci.* **2010**, *257*, 887-898.

(77) Gray, B. M.; Hector, A. L.; Jura, M.; Owen, J. R.; Whittam, J. Effect of Oxidative Surface Treatments on Charge Storage at Titanium Nitride Surfaces for Supercapacitor Applications. *J. Mater. Chem. A* **2017**, *5*, 4550-4559.

(78) Cheng, H.; Ye, J. W.; Sun, Y.; Yuan, W. J.; Tian, J. Y.; Bogale, R. F.; Tian, P.; Ning, G. L. Template-induced Synthesis and Superior Antibacterial Activity of Hierarchical Ag/TiO_2 Composites. *Rsc Adv.* **2015**, *5*, 80668-80676.

(79) Sing, K. S. W.; Everett, D. H.; Haul, R. A. W.; Moscou, L.; Pierotti, R. A.; Rouquerol, J.; Siemieniewska, T. Reporting Physisorption Data for Gas/Solid Systems with Special Reference to the Determination of Surface Area and Porosity. *Pure Appl. Chem.* **1985**, *57*, 603-619.

(80) Puziy, A. M.; Poddubnaya, O. I.; Martinez-Alonso, A.; Suarez-Garcia, F.; Tascon, J. M. D. Synthetic Carbons Activated with Phosphoric Acid II. Porous Structure. *Carbon* **2002**, *40*, 1507-1519.

(81) Tseng, R.-L.; Tseng, S.-K. Pore Structure and Adsorption Performance of the KOH-activated Carbons Prepared from Corncob. *J. Colloid Interface Sci.* **2005**, *287*, 428-437.

(82) Li, H.; Shen, F.; Luo, W.; Dai, J.; Han, X.; Chen, Y.; Yao, Y.; Zhu, H.; Fu, K.; Hitz, E.; Hu, L. Carbonized-leaf Membrane with Anisotropic Surfaces for Sodium-ion Battery. *ACS Appl. Mater. Interfaces* **2016**, *8*, 2204-2210.

(83) Liu, H.; Jia, M.; Yue, S.; Cao, B.; Zhu, Q.; Sun, N.; Xu, B. Creative Utilization of Natural Nanocomposites: Nitrogen-rich Mesoporous Carbon for a High-Performance Sodium Ion Battery. *J. Mater. Chem. A* **2017**, *5*, 9572-9579.

(84) Li, H.; Wang, Q.; Shi, L.; Chen, L.; Huang, X. Nanosized SnSb Alloy Pinning on Hard Non-Graphitic Carbon Spherules as Anode Materials for a Li Ion Battery. *Chem. Mater.* **2002**, *14*, 103-108.

(85) Wang, Y.; Fu, Z.-W.; Yue, X.-L.; Qin, Q.-Z. Electrochemical Reactivity Mechanism of Ni_3N with Lithium. *J. Electrochem. Soc.* **2004**, *151*, E162.

(86) Ghimire, P. C.; Schweiss, R.; Scherer, G. G.; Wai, N.; Lim, T. M.; Bhattarai, A.; Nguyen, T. D.; Yan, Q. Titanium Carbide-decorated Graphite Felt as High Performance Negative Electrode in Vanadium Redox Flow Batteries. *J. Mater. Chem. A* **2018**, *6*, 6625-6632.

(87) Cao, S.; Xue, Z.; Yang, C.; Qin, J.; Zhang, L.; Yu, P.; Wang, S.; Zhao, Y.; Zhang, X.; Liu, R. Insights into the Li^+ Storage Mechanism of TiC@C-TiO_2 Core-shell Nanostructures as High Performance Anodes. *Nano Energy* **2018**, *50*, 25-34.

(88) Liu, Y.; Liu, L.; Kong, L.; Kang, L.; Ran, F. Supercapacitor Electrode Based on Nano-vanadium Nitride Incorporated on Porous Carbon Nanospheres Derived from Ionic Amphiphilic Block Copolymers & Vanadium-contained Ion Assembly Systems. *Electrochim. Acta* **2016**, *211*, 469-477.